

Scanning-probe and information-concealing machine learning intermediate hexatic phase and critical scaling of solid-hexatic phase transition in deformable particles

Wei-chen Guo, Bao-quan Ai,* and Liang He†

*Guangdong Provincial Key Laboratory of Quantum Engineering and Quantum Materials,
School of Physics and Telecommunication Engineering,
South China Normal University, Guangzhou 510006, China and
Guangdong-Hong Kong Joint Laboratory of Quantum Matter,
South China Normal University, Guangzhou 510006, China*

We investigate the two-dimensional melting of deformable polymeric particles with multi-body interactions described by the Voronoi model. We report machine learning evidence for the existence of the intermediate hexatic phase in this system, and extract the critical exponent $\nu \approx 0.65$ for the divergence of the correlation length of the associated solid-hexatic phase transition. Moreover, we clarify the discontinuous nature of the hexatic-liquid phase transition in this system. These findings are achieved by directly analyzing system's spatial configurations with two generic machine learning approaches developed in this work, dubbed “scanning-probe” via which the possible existence of intermediate phases can be efficiently detected, and “information-concealing” via which the critical scaling of the correlation length in the vicinity of generic continuous phase transition can be extracted. Our work provides new physical insights into the fundamental nature of the two-dimensional melting of deformable particles, and establishes a new type of generic toolbox to investigate fundamental properties of phase transitions in various complex systems.

Introduction.—The nature of two-dimensional (2D) melting [1] is delicate and can show non-trivial dependence on several properties of the specific systems, e.g., softness [2, 3], activity [4–8], density [9], potential [10–14], pinning of particles [15], shape of particles [16, 17], topological constraints [18], etc. Three different types of 2D melting scenarios, namely, the one-step melting scenario [19], the hard-disk-like scenario [20–22], and the Kosterlitz-Thouless-Halperin-Nelson-Young scenario [23–26] have been identified. However, some questions are still left open. The most important ones include the existence of the intermediate hexatic phase and the fundamental nature of its associated phase transitions.

To solve these open questions, one crucial step is to identify different phases in the relevant systems. This is usually done via investigating the spatial decay of correlation functions of the translational order and the bond-orientational order, combined with the unbinding behavior of dislocations and disclinations [23–26]. More specifically, it is suggested that the solid-hexatic phase transition is associated with the disappearance of the quasi-long range translational order and the increasing number of dislocations [2], and that the hexatic-liquid phase transition is associated with the disappearance of the long range bond-orientational order and the dissociation of the dislocation into disclinations [2]. However, a firm confirmation within this approach is still difficult, partially due to the possibly enormous value of the hexatic correlation length [12] and also the fact that other complicated defects, such as vacancies and grain boundaries, might appear near the phase transitions [27–29]. Noticing that machine learning techniques have emerged

in recent years as an efficient tool to investigate various problems on phase transitions [30–48], this thus raises the intriguing opportunity to develop new tools based on these powerful techniques to reveal new physical insights into these open questions, in particular, the ones concerning the existence of the intermediate hexatic phase and the fundamental nature of its associated phase transitions, especially the possible critical scaling behavior.

In this work, we address these questions for the 2D melting of deformable polymeric particles with multi-body interactions described by the Voronoi model [2, 49–54]. To this end, we develop two generic neural network-based machine learning approaches dubbed “scanning-probe” [cf. Fig. 1(a)] and “information-concealing” [cf. Fig. 2(a)] to directly analyze a large number of system's spatial configurations that are generated by Brownian dynamics simulations, and find the following.

(i) Machine learning evidence for the existence of the intermediate hexatic phase (cf. Fig. 1). At the low temperature, when the so-called target shape index of the system increases, the classification accuracy [cf. Eq. (3)] associated with the “phase-transition-probe” manifests two pronounced peaks that signify two phase transitions and hence three distinct phases, with the intermediate one corresponding to the hexatic phase [cf. Fig. 1(b)]. At the relatively high temperature, the single peak behavior of the classification accuracy of the “phase-transition-probe”, combined with the phase coexistence region identified by an auxiliary machine learning, still indicates the existence of three distinct phases with the intermediate one corresponding to the hexatic phase [cf. Fig. 1(c)]. The identified phase coexistence region also clarifies the discontinuous nature of the hexatic-liquid phase transition in this system.

(ii) The continuous solid-hexatic phase transition manifests a critical scaling behavior with the critical expo-

* aibq@sclu.edu.cn

† liang.he@sclu.edu.cn

ment $\nu \approx 0.65$ for the divergence of the correlation length (cf. Fig. 2). We observe that at different temperatures, the good data collapse is achieved for the average outputs of the convolutional neural network (CNN) employed in “information-concealing” machine learning as a function of the reduced target shape index when it is rescaled with the critical exponent $\nu \approx 0.65$ [cf. Figs. 2(c), 2(e)] with respect to the linear size l of the system after “concealing”, clearly manifesting the critical scaling behavior of the correlation length in the vicinity of the continuous solid-hexatic phase transition.

System and model.—The system under study consists of N deformable polymeric particles with multi-body interactions [2], whose elastic energy E is modeled according to the Voronoi description [49–54],

$$E(\{\mathbf{r}_i\}) = \sum_{i=1}^N [K_A(A_i - A_0)^2 + K_P(P_i - P_0)^2], \quad (1)$$

where A_i and P_i are the cross-sectional area and the perimeter of the i th particle, A_0 and P_0 are the preferred particle area and perimeter, K_A and K_P represent the area and perimeter stiffness moduli, respectively. This Voronoi model originates from the investigations of the confluent cells in biological tissues, where the first term in Eq. (1) models the cell incompressibility and the monolayer’s resistance to height fluctuations, and the second term arises from the active contractility of the actomyosin subcellular cortex and the effective cell membrane tension due to the cell-cell adhesion and cortical tension. The effective dimensionless target shape index $p_0 = P_0/\sqrt{A_0}$ is an important parameter that controls the elastic behavior of these deformable particles. The elastic energy in Eq. (1) leads to a mechanical interaction force on the i th particle by $\mathbf{F}_i = -\nabla_{\mathbf{r}_i} E(\{\mathbf{r}_i\})$, which is a multi-body interaction force that cannot be expressed as a sum of pairwise force between the i th particle and its neighbors [49–54]. To simulate the dynamics in this system, each particle undergoes overdamped Brownian motion at a given temperature T . Thus, the dynamics of the deformable particles in the overdamped limit follows the Langevin equation [49–54]

$$\frac{d\mathbf{r}_i}{dt} = \mu \mathbf{F}_i + \sqrt{2\mu k_B T} \boldsymbol{\xi}_i(t), \quad (2)$$

where μ is the mobility, k_B is the Boltzmann constant, and $\boldsymbol{\xi}_i(t)$ are Gaussian white noises with zero mean and unit variance. Equations (1), (2) can be rewritten in the dimensionless forms by introducing the characteristic length $\sqrt{A_0}$ and time $1/(\mu K_A A_0)$. The parameters in the dimensionless forms can be rewritten as $\hat{K}_P = K_P/(K_A A_0)$ and $\hat{T} = k_B T/(K_A A_0^2)$. We shall omit the hat for all quantities occurring in the above equations from now on and use only the dimensionless variables.

From the expression for the elastic energy in Eq. (1), we can see that at fixed temperature T , the system softens when the target shape index p_0 increases. Therefore,

(a) Scanning-probe

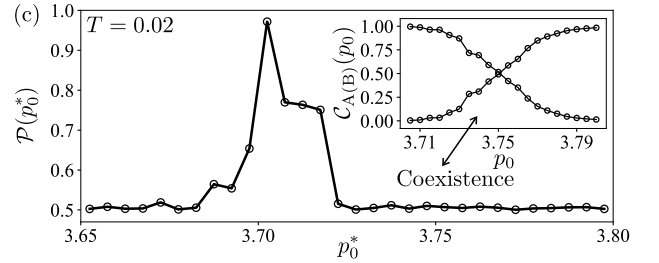
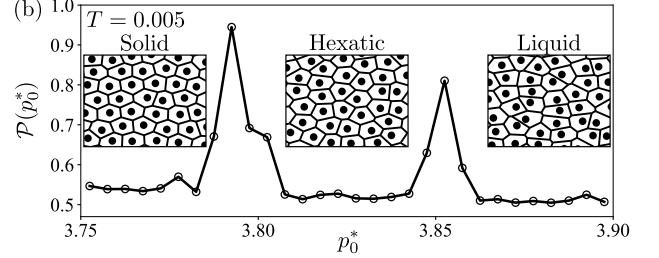
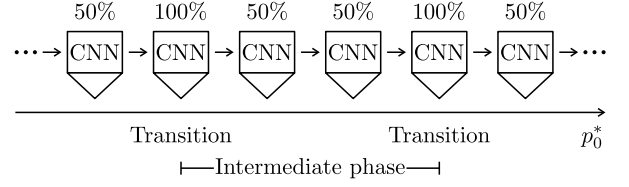


Figure 1. (a) Schematic illustration of “scanning-probe” machine learning. The “phase-transition-probe” is realized by a deep CNN that is able to give the signal $\mathcal{P}(p_0^*)$ on how likely there is a phase transition in a narrow parameter interval $[p_0^* - \Delta p_0, p_0^* + \Delta p_0]$, where $\mathcal{P}(p_0^*) \approx 100\%$ indicates the existence of a possible transition, with p_0^* being the suspected phase transition point and Δp_0 being the resolution of the probe. (b) Identification of the intermediate hexatic phase at a low temperature $T = 0.005$. The classification accuracy $\mathcal{P}(p_0^*)$ associated with the “phase-transition-probe” manifests two pronounced peaks that signify two phase transitions and hence three distinct phases, with the intermediate one corresponding to the hexatic phase. And these double peaks correspond to the solid-hexatic phase transition point $p_0^{\text{SH}} = 3.7925 \pm 0.0025$ and the hexatic-liquid phase transition point $p_0^{\text{HL}} = 3.8525 \pm 0.0025$, respectively. Inset: Typical samples of the data in the solid phase (left), the hexatic phase (middle), and the liquid phase (right). (c) Identification of the intermediate hexatic phase at a relatively high temperature $T = 0.02$. The classification accuracy $\mathcal{P}(p_0^*)$ associated with “phase-transition-probe” manifests only a single peak in this case, and this peak corresponds to the solid-hexatic phase transition point with $p_0^{\text{SH}} = 3.7025 \pm 0.0025$. Inset: The auxiliary machine learning to resolve the hexatic-liquid phase coexistence. Two average confidence values $C_{A(B)}(p_0)$ of the deep CNN show big differences around 100% in the vicinities of both ends of the parameter interval $[3.705, 3.800]$ for p_0 , clearly indicating that there exist two distinct phases around $p_0 = 3.705$ and $p_0 = 3.800$, i.e., the hexatic phase and the liquid phase. The parameter region around the intersection point is expected to correspond to a phase coexistence region of these two phases, and the upper bound for the hexatic phase region can be estimated by this point with $p_0^{\text{H,UB}} = 3.7507$. See text for more details.

one naturally expects a solid phase with small p_0 , and a liquid phase with large p_0 . With an intermediate p_0 , one so-called hexatic phase could possibly emerge as an intermediate phase between the solid and the liquid phases. Recent investigations [2–4, 49–54] have shown numerical evidence that supports the existence of the intermediate hexatic phase in this system from properties of the translational correlation function, the bond-orientational correlation function, and different types of topological defects such as dislocations and disclinations. However, potential limitations of the existing evidence were also reported, for instance, the exponent of the asymptotic power law decay of the correlation functions can be difficult to extract due to the limited system size employed in the study [5, 12], and the relevant types of topological defects that drive the phase transition associated with the intermediate hexatic phase are still under debate [27–29]. In this regard, a type of approaches that directly analyzes the system’s spatial configurations with as few build-in empirical assumptions as possible is highly desirable to provide new physical insights into the questions concerning the existence of the intermediate hexatic phase and the fundamental nature of its associated phase transitions in this system. Indeed, as we shall see in the following sections, such a type of approaches can be developed by utilizing the modern machine learning techniques [55, 56].

Here in this work, we focus on the case with $K_P = 1$, and set the particle number $N = 3960$ (cf. Supplemental Material [66] for an investigation on the finite size effect, which shows that it does not impose strong influences on the major results presented in the following). The configurations to be directly processed by the machine learning approaches developed in the following are obtained by Brownian dynamics simulations of the system in a 2D rectangular space with aspect ratio $2/\sqrt{3}$ and periodic boundary condition imposed. The initial configuration is chosen to be a perfect hexagonal lattice. With different fixed values for (T, p_0) , we typically generate 2×10^3 of system’s spatial configurations in the steady state, and transform these configurations into images according to the Voronoi tessellation [49–54] (see Supplemental Material [66] for more technical details on the data generation).

Intermediate hexatic phase identified via “scanning-probe”.—To identify the intermediate hexatic phase, we need a high-resolution machine learning approach to efficiently detect multiple phase transitions triggered by tuning a single system parameter, in contrast to most of the well-established machine learning approaches that are experts in searching for a single phase transition in a large parameter region [31, 32]. Here, we develop a generic machine learning approach dubbed “scanning-probe”, in which the key workhorse is a “phase-transition-probe” that is able to give the signal on how likely there is a phase transition in a narrow parameter interval $[p_0^* - \Delta p_0, p_0^* + \Delta p_0]$ with p_0^* being the suspected phase transition point and Δp_0 being the resolution of the probe. Since the hexatic phase can be far from obvious

in the real space [cf. insets of Fig. 1(b)], the “scanning-probe” approach can be realized by a deep CNN that has strong feature extraction ability, where the network is trained as a binary classifier by using the data associated with the two boundaries of the interval. More specifically, we label all the samples with $p_0 = p_0^* - \Delta p_0$ as “phase A” and the ones with $p_0 = p_0^* + \Delta p_0$ as “phase B”, and the probe’s signal concerning the phase transition is given by the classification accuracy $\mathcal{P}(p_0^*)$ in the testing process of the trained CNN, whose explicit form reads

$$\mathcal{P}(p_0^*) \equiv \frac{M_A^- + M_B^+}{2M}, \quad (3)$$

with M being the number of test samples associated with each p_0 and M_A^- (M_B^+) being the number of test samples that have been identified successfully as phase A (B) by the CNN. Here, the CNN gives two outputs (y_A, y_B) , where $y_{A(B)}$ can be regarded as a classification confidence value $\in [0, 1]$ of how likely the sample is in phase A (B). For a sample fed to the CNN, it is identified as phase A if $y_A > y_B$ or phase B if $y_A < y_B$. As one can naturally expect if the two groups of data belong to the same phase physically, there should be no essential difference between each other, hence the CNN can only learn to trivially identify all the samples as the same phase. This leads to either $(M_A^-, M_B^+) \approx (M, 0)$ or $(M_A^-, M_B^+) \approx (0, M)$, i.e., $\mathcal{P}(p_0^*) \approx 50\%$, which is equivalent to a random guess. On the contrary, if there indeed exists a phase transition in the interval $[p_0^* - \Delta p_0, p_0^* + \Delta p_0]$, the two groups of data can naturally manifest certain distinct differences from each other that can be learned by the CNN, hence the classification accuracy is expected to be very high, i.e., $\mathcal{P}(p_0^*) \approx 100\%$, which can be used as a clear signal for the phase transition point (see Supplemental Material [66] for more technical details on the network training).

Via making a scanning with the “phase-transition-probe” over the complete parameter region of interests, possible phase transitions in it can be detected. Since each probing involves only two groups of data that correspond to $p_0^* - \Delta p_0$ and $p_0^* + \Delta p_0$, the computational cost of the “scanning-probe” approach scales linearly with respect to the number of the suspected parameter points in the complete parameter region. This is in contrast to the machine learning approaches that employ all the data, e.g., the confusion scheme [32], whose the computational cost scales quadratically with respect to the number of the suspected parameter points.

We first consider a nearly zero-temperature case at $T = 0.005$. As we can see from Fig. 1(b), the p_0^* dependence of $\mathcal{P}(p_0^*)$ manifests two pronounced peaks, indicating that there should exist three distinct phases in this system. From the expression of the system’s elastic energy in Eq. (1), we know that the system becomes harder as the target shape index p_0 becomes smaller, hence the system with a very small target shape index p_0 is expected to be in the solid phase. Combining this physical understanding with the behavior that $\mathcal{P}(p_0^*) \approx 50\%$ on the left side of the left peak in Fig. 1(b), which manifests

that the system’s spatial configurations associated with the small interval $[p_0^* - \Delta p_0, p_0^* + \Delta p_0]$ show no significant difference among them, we can conclude that the system is solid if p_0 is smaller than the target shape index value corresponding to the left peak. In contrast, the system with a very large p_0 should be in the liquid phase, since the increase of p_0 favors less compact shapes and thus a reduction in the number of sides of the Voronoi tessellation [2–4, 49–54]. Combining with the fact that $\mathcal{P}(p_0^*) \approx 50\%$ on the right side of the right peak in Fig. 1(b), we can conclude that the system is liquid if p_0 is larger than the target shape index value corresponding to the right peak. In this regard, one can naturally arrive at a further conclusion that an intermediate phase exists between the two peaks, which is neither the solid phase nor the liquid phase, and is expected to be the intermediate hexatic phase that emerges between the solid and the liquid phases in 2D systems. Consequently, the left peak in Fig. 1(b) corresponds to the solid-hexatic phase transition point with $p_0^{\text{SH}} = 3.7925 \pm 0.0025$, while the right one corresponds to the hexatic-liquid phase transition point with $p_0^{\text{HL}} = 3.8525 \pm 0.0025$, which is consistent with the phase transition points $p_0^{\text{SH}} \approx 3.78$ and $p_0^{\text{HL}} \approx 3.85$ at $T = 0.005$ identified via conventional approaches [2], providing strong machine learning evidence for the existence of the intermediate hexatic phase.

We further investigate a relatively high temperature case at $T = 0.02$. In this case, the deep CNN detects only a single peak, as shown in Fig. 1(c). This seems to imply that there exist only two phase at this temperature. However, we note that the signal of the “phase-transition-probe” [cf. Eq. (3)] is associated with a narrow parameter interval $[p_0^* - \Delta p_0, p_0^* + \Delta p_0]$. If there exists a strong phase coexistence in the certain parameter region, as ubiquitous in the vicinities of the first-order phase transitions, the probe indeed can also give the signal $\mathcal{P}(p_0^*) \approx 50\%$ in this parameter region despite possible first-order phase transitions could exist. Therefore, the single peak in Fig. 1(c) might also indicate that there exists a relatively large phase coexistence parameter region on its right. This motivates us to perform an auxiliary machine learning, where we train the CNN using the data associated with two parameter points that are well separated from each other. More specifically, we use the data with $p_0 = 3.705$ and $p_0 = 3.800$, and label all the samples associated with the former as “phase A” and the latter as “phase B”. We then test the average confidence values ($\mathcal{C}_A, \mathcal{C}_B$) of the trained CNN for $p_0 \geq 3.705$, where $\mathcal{C}_{A(B)} \equiv \langle y_{A(B)} \rangle$ and $\langle \cdot \rangle$ denotes the average over M test samples associated with each p_0 . As we can see from the inset of Fig. 1(c), the average outputs ($\mathcal{C}_A, \mathcal{C}_B$), i.e., the average classification confidence values associated with phase A and phase B, show big differences around 100% in the vicinities of both ends of the parameter interval $[3.705, 3.800]$ for p_0 . This clearly indicates that there indeed exist two distinct phases around $p_0 = 3.705$ and $p_0 = 3.800$, and thus the parameter region around the intersection point in the inset of Fig. 1(c) is expected to correspond to a

phase coexistence region. From the expression of the system’s elastic energy in Eq. (1), we know that the systems with the small p_0 on the left side of the peak are in the solid phase. While the intersection point in the inset of Fig. 1(c) appears far right of the peak, so the phase coexistence around the intersection point is not relevant to the solid phase, but should be a coexistence between the hexatic and the liquid phases. Therefore, we can conclude that the peak in Fig. 1(c) corresponds to the solid-hexatic phase transition point $p_0^{\text{SH}} = 3.7025 \pm 0.0025$, which is also consistent with the phase transition point $p_0^{\text{SH}} \approx 3.69$ at $T = 0.02$ identified via conventional approaches [2], and that the intersection point in the inset of Fig. 1(c) should correspond to an upper bound of the hexatic phase region with $p_0^{\text{H,UB}} = 3.7507$. Moreover, the existence of this relatively large phase coexistence region naturally leads to the conclusion that the hexatic-liquid phase transition in this system is discontinuous.

Critical scaling extracted via “information-concealing”.—So far, we have identified the intermediate hexatic phase and clarified the discontinuous nature of the hexatic-liquid phase transition. One fundamental question still left is the critical scaling of the solid-hexatic phase transition. To address this question, we develop a generic machine learning approach dubbed “information-concealing” that is able to extract the critical scaling of the correlation length in the vicinity of a generic continuous phase transition.

This approach is based on the natural expectation that for a CNN employed to perform a classification task in a translational invariant way, its outputs, i.e., the classification confidence values, shall be dominated by the features whose characteristic length scales are given by the correlation length ξ of the system. This thus indicates that the content of the effective information of each sample of the data, which the CNN can utilize to perform the classification task, is determined by a characteristic ratio $\lambda \equiv l/\xi$ with l being the length scale of the effective area of the sample [cf. Fig. 2(a)]. Consequently, for two different samples, as long as their characteristic ratios λ are the same, their corresponding average confidence values of the CNN are expected to be the same, too. This directly indicates that for a generic continuous phase transition triggered by tuning a system parameter g across its critical value g_c , the average confidence values as a function of the rescaled system parameter $(g - g_c)l^{1/\nu}$ with different fixed l should collapse to the same universal function near the phase transition, since the correlation length ξ generically manifests the power law behavior $\xi \propto (g - g_c)^{-\nu}$ in the vicinity of the continuous phase transition with ν being the critical exponent for the divergence of the correlation length. Therefore, the critical exponent ν can be determined according to the data collapse behavior of the average confidence values as a function of the rescaled system parameter $(g - g_c)l^{1/\nu}$ with different fixed l .

To implement the “information-concealing” approach, the information of the samples in the original dataset are

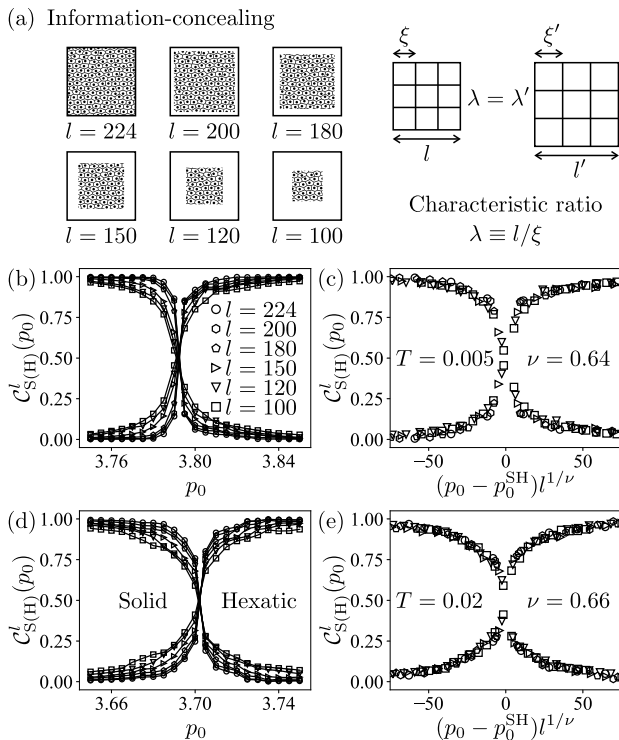


Figure 2. (a) Schematic illustration of “information-concealing” machine learning. The peripheries of the samples in the original dataset are deliberately concealed to generate a series of datasets with reduced effective areas characterized by the effective length scale l for their samples. The ratio between l and the system correlation length $\xi(p_0)$, i.e., $\lambda = l/\xi(p_0)$, determines the information content of the system that can be utilized by the CNN to perform the classification task. For instance, a small sample with linear size l and a correlation length $\xi(p_0)$ is expected to contain the same amount of information for the CNN as a larger sample with linear size l' and a larger correlation length $\xi(p'_0)$ if $l/\xi(p_0) = l'/\xi(p'_0)$. This indicates that the critical exponent ν for the divergence of the correlation length can be extracted via the data collapse behavior of the average confidence values that performs the classification task with respect to datasets with samples of effective length scale l . (b) Average confidence values of the CNN to classify the hexatic phase from the solid phase using datasets with different fixed l at the low temperature $T = 0.005$. (c) The good data collapse is achieved for the average confidence values in (b) as a function of $(p_0 - p_0^{\text{SH}})l^{1/\nu}$ with the critical exponent $\nu = 0.64$. (d) Average confidence values of the CNN to classify the hexatic phase from the solid phase using datasets with different fixed l at the relatively high temperature $T = 0.02$. (e) The good data collapse is achieved for the average confidence values in (d) as a function of $(p_0 - p_0^{\text{SH}})l^{1/\nu}$ with the critical exponent $\nu = 0.66$. See text for more details.

deliberately concealed to generate a series of datasets with reduced effective areas for their samples. Each of these samples with reduced effective areas is obtained by randomly choosing an area of $l \times l$ pixels from the original images and conceal its periphery with the white color [cf. Fig. 2(a)]. The critical scaling of the correla-

tion length ξ in the vicinity of the phase transition under consideration is then straightforwardly obtained by investigating the data collapse behavior of the average confidence values as a function of the rescaled system parameter $(g - g_c)l^{1/\nu}$ with different fixed l (see Supplemental Material [66] for more technical details). A benchmark of this approach is presented in Supplemental Material [66], where a good estimation of the critical exponent $\nu_1 = 1.04$ (exact value $\nu_1 = 1$ [57]) for the ferromagnetic-paramagnetic transition of the 2D Ising model is obtained.

We directly apply this “information-concealing” approach to reveal the critical scaling of the solid-hexatic phase transition in deformable particles with the CNN employed to perform the classification tasks. More specifically, we first perform “concealing” with a choice of effective length scale l to generate the corresponding dataset. Then, this complete dataset is used to train the CNN to perform the classification between the solid and the hexatic phases. After training, the CNN is able to output the classification confidence values (y_S, y_H) concerning the samples with corresponding target shape index p_0 , i.e., establish a map between the average confidence values (C_S, C_H), where $C_{S(H)} \equiv \langle y_{S(H)} \rangle$, and the target shape index p_0 , from which the phase transition point p_0^{SH} is identified by the p_0 where $C_S(p_0) = C_H(p_0)$. We repeat this process with a series of different choices of the effective length scale $l = 224, 200, 180, 150, 120, 100$, and get the corresponding $C_S^l(p_0)$ and $C_H^l(p_0)$. Fig. 2(b) shows the dependence of the average confidence values on p_0 with different fixed l at the low temperature $T = 0.005$, where the behaviors differ with respect to the target shape index p_0 . However, $C_{S(H)}^l$ indeed shows the same dependence on its rescaled target shape index $(p_0 - p_0^{\text{SH}})l^{1/\nu}$ with $\nu = 0.64$, as shown in Fig. 2(c), indicating that the critical exponent ν for the divergence of the correlation length of the solid-hexatic phase transition assumes the value $\nu = 0.64$. We further perform the similar investigation at the relatively high temperature $T = 0.02$, the key results of which are shown in Figs. 2(d), (e), where we notice that the good data collapse for the average confidence values is observed for $\nu = 0.66$. This is consistent with the value of the critical exponent obtained at $T = 0.005$, indicating that the critical scaling of the correlation length ξ in the vicinity of the solid-hexatic phase transition is given by the power law $\xi \propto (p_0 - p_0^{\text{SH}})^{-\nu}$ with $\nu \approx 0.65$.

Finally, we remark that both “scanning-probe” and “information-concealing” machine learning involve no special design of the CNN structure. A widely-used standard 18-layer residual neural network [58] is employed to perform the analysis as shown in Fig. 1 and Fig. 2 in the main text. In Supplemental Material [66], we present the same analysis employing another type of deep CNN called “GoogLeNet” [59], which gives the same results as the ones obtained by the residual neural network. This clearly shows the CNN structure independence of the two approaches developed in this work, which is indis-

pensable for the reliability of the physical results they predict. Moreover, this also indicates the wide generic applicability of these approaches in investigating other relevant complex systems.

Conclusion and outlook.—By directly analyzing system’s spatial configurations via “scanning-probe” and “information-concealing” machine learning developed in this work, we provide machine learning evidence for the existence of the intermediate hexatic phase in 2D interacting deformable polymeric particles, and obtained the critical scaling behavior of the solid-hexatic phase transition, where the divergence of the correlation length is determined by a power law with the critical exponent $\nu \approx 0.65$. Since these two machine learning approaches involve no special design for the CNN employed, they can be readily employed as a new generic toolbox to investigate the existence of the intermediate phase and the possible critical scaling behavior in various complex systems. For instance, we believe that our work will stimulate further efforts in revealing the critical scaling behavior of the

solid-hexatic phase transition in nonequilibrium complex systems, e.g., in self-propelled biological tissues, via these new approaches. Moreover, noticing that the deep CNNs employed here are in general quite powerful in pattern recognition, we also expect that our machine learning approaches can be applied to investigate the physics associated with 2D microphase separations [62–65] in various complex systems.

ACKNOWLEDGMENTS

We thank Jiajian Li for useful discussions. This work was supported by NSFC (Grant No. 11874017 and No. 12075090), GDSTC (Grant No. 2018A030313853 and No. 2017A030313029), GDUPS (2016), Major Basic Research Project of Guangdong Province (Grant No. 2017KZDXM024), Science and Technology Program of Guangzhou (Grant No. 2019050001), and START grant of South China Normal University.

-
- [1] K. J. Strandburg, *Rev. Mod. Phys.* **60**, 161 (1988).
 - [2] Y.-W. Li and M. P. Ciamarra, *Phys. Rev. Mater.* **2**, 045602 (2018).
 - [3] M. Durand and J. Heu, *Phys. Rev. Lett.* **123**, 188001 (2019).
 - [4] A. Pasupalak, Y.-W. Li, R. Ni, and M. P. Ciamarra, *Soft Matter* **16**, 3914 (2020).
 - [5] Y. Komatsu and H. Tanaka, *Phys. Rev. X* **5**, 031025 (2015).
 - [6] P. Digregorio, D. Levis, A. Suma, L. F. Cugliandolo, G. Gonnella, and I. Pagonabarraga, *Phys. Rev. Lett.* **121**, 098003 (2018).
 - [7] J. U. Klamsner, S. C. Kapfer, and W. Krauth, *Nat. Commun.* **9**, 5045 (2018).
 - [8] J. U. Klamsner, S. C. Kapfer, and W. Krauth, *J. Chem. Phys.* **150**, 144113 (2019).
 - [9] M. Zu, J. Liu, H. Tong, and N. Xu, *Phys. Rev. Lett.* **117**, 085702 (2016).
 - [10] S. C. Kapfer and W. Krauth, *Phys. Rev. Lett.* **114**, 035702 (2015).
 - [11] B. Li, F. Wang, D. Zhou, Y. Peng, R. Ni, and Y. Han, *Nature* **531**, 485 (2016).
 - [12] Y.-W. Li and M. P. Ciamarra, *Phys. Rev. Lett.* **124**, 218002 (2020).
 - [13] A. Hajibabaei and K. S. Kim, *Phys. Rev. E* **99**, 022145 (2019).
 - [14] P. Bladon and D. Frenkel, *Phys. Rev. Lett.* **74**, 2519 (1995).
 - [15] S. Deuschländer, T. Horn, H. Löwen, G. Maret, and P. Keim, *Phys. Rev. Lett.* **111**, 098301 (2013).
 - [16] J. A. Anderson, J. Antonaglia, J. A. Millan, M. Engel, and S. C. Glotzer, *Phys. Rev. X* **7**, 021001 (2017).
 - [17] L. F. Cugliandolo, P. Digregorio, G. Gonnella, and A. Suma, *Phys. Rev. Lett.* **119**, 268002 (2017).
 - [18] R. E. Guerra, C. P. Kelleher, A. D. Hollingsworth, and P. M. Chaikin, *Nature* **554**, 346 (2018).
 - [19] D. R. Nelson, *Phys. Rev. B* **18**, 2318 (1978).
 - [20] E. P. Bernard and W. Krauth, *Phys. Rev. Lett.* **107**, 155704 (2011).
 - [21] J. Russo and N. B. Wilding, *Phys. Rev. Lett.* **119**, 115702 (2017).
 - [22] A. L. Thorneywork, J. L. Abbott, D. G. A. L. Aarts, and R. P. A. Dullens, *Phys. Rev. Lett.* **118**, 158001 (2017).
 - [23] J. M. Kosterlitz and D. J. Thouless, *J. Phys. C* **6**, 1181 (1973).
 - [24] B. I. Halperin and D. R. Nelson, *Phys. Rev. Lett.* **41**, 121 (1978).
 - [25] D. R. Nelson and B. I. Halperin, *Phys. Rev. B* **19**, 2457 (1979).
 - [26] A. P. Young, *Phys. Rev. B* **19**, 1855 (1979).
 - [27] P. Digregorio, D. Levis, L. F. Cugliandolo, G. Gonnella, and I. Pagonabarraga, arXiv:2106.03454.
 - [28] W. Qi, A. P. Gantapara, and M. Dijkstra, *Soft Matter* **10**, 5449 (2014).
 - [29] M. A. Bates and D. Frenkel, *Phys. Rev. E* **61**, 5223 (2000).
 - [30] P. Broecker, F. F. Assaad, and S. Trebst, arXiv:1707.00663.
 - [31] J. Carrasquilla and R. G. Melko, *Nat. Phys.* **13**, 431 (2017).
 - [32] E. P. L. van Nieuwenburg, Y.-H. Liu, and S. D. Huber, *Nat. Phys.* **13**, 435 (2017).
 - [33] P. Broecker, J. Carrasquilla, R. G. Melko, and S. Trebst, *Sci. Rep.* **7**, 8823 (2017).
 - [34] L. Wang, *Phys. Rev. B* **94**, 195105 (2016).
 - [35] S. S. Lee and B. J. Kim, *Phys. Rev. E* **99**, 043308 (2019).
 - [36] K. Shinjo, S. Sota, S. Yunoki, and T. Tohyama, *Phys. Rev. B* **101**, 195136 (2020).
 - [37] K. Kottmann, P. Huembeli, M. Lewenstein, and A. Acín, *Phys. Rev. Lett.* **125**, 170603 (2020).
 - [38] W. Rządkowski, N. Defenu, S. Chiacchiera, A. Trombetti, and G. Bighin, *New J. Phys.* **22**, 093026 (2020).
 - [39] W.-C. Guo, B.-Q. Ai, and L. He, arXiv:2005.10505.
 - [40] W.-C. Guo, B.-Q. Ai, and L. He, *Phys. Rev. E* **104**,

- 044611 (2021).
- [41] N. Maskara, M. Buchhold, M. Endres, and E. P. L. van Nieuwenburg, arXiv:2103.15855.
- [42] H. Li, Y. Jin, Y. Jiang, and J. Z. Y. Chen, Proc. Natl. Acad. Sci. U.S.A. **118**, e2017392118 (2021).
- [43] M. Koch-Janusz and Z. Ringel, Nat. Phys. **14**, 578 (2018).
- [44] D. E. Gökmen, Z. Ringel, S. D. Huber, and M. Koch-Janusz, Phys. Rev. E **104**, 064106 (2021).
- [45] S. Efthymiou, M. J. S. Beach, and R. G. Melko, Phys. Rev. B **99**, 075113 (2019).
- [46] Z. Li, M. Luo, and X. Wan, Phys. Rev. B **99**, 075418 (2019).
- [47] W. Zhang, J. Liu, and T.-C. Wei, Phys. Rev. E **99**, 032142 (2019).
- [48] D. Bachtis, G. Aarts, and B. Lucini, Phys. Rev. E **102**, 033303; 053306 (2020).
- [49] D. M. Sussman, J. M. Schwarz, M. C. Marchetti, and M. L. Manning, Phys. Rev. Lett. **120**, 058001 (2018).
- [50] D. Bi, J. H. Lopez, J. M. Schwarz, and M. L. Manning, Nat. Phys. **11**, 1074 (2015).
- [51] D. Bi, X. Yang, M. C. Marchetti, and M. L. Manning, Phys. Rev. X **6**, 021011 (2016).
- [52] F. Giavazzi, M. Paoluzzi, M. Macchi, D. Bi, G. Scita, M. L. Manning, R. Cerbino, and M. C. Marchetti, Soft Matter **14**, 3471 (2018).
- [53] D. M. Sussman, Comput. Phys. Commun. **219**, 400 (2017).
- [54] S. Henkes, K. Kostanjevec, J. M. Collinson, R. Sknepnek, and E. Bertin, Nat. Commun. **11**, 1405 (2020).
- [55] M. A. Nielsen, *Neural Networks and Deep Learning*, Determination Press (2015).
- [56] I. Goodfellow, Y. Bengio, and A. Courville, *Deep Learning*, MIT Press (2016).
- [57] J. B. Kogut, Rev. Mod. Phys. **51**, 659 (1979).
- [58] K. He, X. Zhang, S. Ren, and J. Sun, Proc. of IEEE CVPR, 770 (2016).
- [59] C. Szegedy, W. Liu, Y. Jia, P. Sermanet, S. Reed, D. Anguelov, D. Erhan, V. Vanhoucke, and A. Rabinovich, Proc. of IEEE CVPR, 1 (2015).
- [60] D. P. Kingma and J. L. Ba, arXiv:1412.6980.
- [61] P. S. Ruiz, Q.-L. Lei, and R. Ni, Commun. Phys. **2**, 70 (2019).
- [62] B. Liebchen and D. Levis, Phys. Rev. Lett. **119**, 058002 (2017).
- [63] C. B. Caporusso, P. Digregorio, D. Levis, L. F. Cugliandolo, and G. Gonnella, Phys. Rev. Lett. **125**, 178004 (2020).
- [64] Q.-L. Lei, M. P. Ciamarra, and R. Ni, Sci. Adv. **5**, eaau7423 (2019).
- [65] Z. Ma and R. Ni, J. Chem. Phys. **156**, 021102 (2022).
- [66] See Supplemental Material, which includes Refs. [31, 41, 55–61], for (i) technical information about the data generation and the network training, (ii) a benchmark of the “information-concealing” approach, (iii) results that show the CNN structure independence of both approaches developed in this work, and (iv) investigations on influences of the finite size effect and the number of samples in the dataset.

Supplemental Material for “Scanning-probe and information-concealing machine learning intermediate hexatic phase and critical scaling of solid-hexatic phase transition in deformable particles”

Wei-chen Guo, Bao-quan Ai,* and Liang He†

Guangdong Provincial Key Laboratory of Quantum Engineering and Quantum Materials,
School of Physics and Telecommunication Engineering,
South China Normal University, Guangzhou 510006, China and
Guangdong-Hong Kong Joint Laboratory of Quantum Matter,
South China Normal University, Guangzhou 510006, China

This Supplemental Material provides (i) technical information about the data generation and the network training, (ii) a benchmark of the “information-concealing” approach, (iii) results that show the CNN structure independence of both approaches developed in this work, and (iv) investigations on influences of the finite size effect and the number of samples in the dataset.

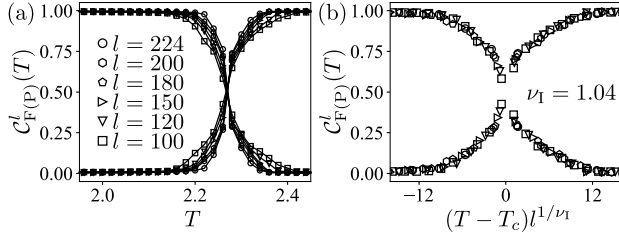


Figure S1. (a) Average confidence values of the CNN to classify the ferromagnetic phase from the paramagnetic phase using datasets with different fixed l of the 2D Ising model without external field. (b) The good data collapse is achieved for the average confidence values in (a) as a function of $(T - T_c)l^{1/\nu_1}$ with the critical exponent $\nu_1 = 1.04$. This is a good estimation of the critical exponent for the divergence of the correlation length of the 2D Ising model (exact value $\nu_1 = 1$). See text for more details.

DATA GENERATION AND NETWORK TRAINING

In this work, for each $p_0 = 3.750, 3.755, \dots, 3.900$ at the low temperature $T = 0.005$, and $p_0 = 3.650, 3.655, \dots, 3.800$ at the relatively high temperature $T = 0.02$, we perform Brownian dynamics simulations for 10^6 time steps with $dt = 0.01$ to equilibrate the system, and confirm it from the convergence of the system’s elastic energy. Afterwards, the dynamics of the system is simulated for additional 10^5 time steps, during which the spatial configuration of the system is sampled every 50 time steps. These configurations are transformed to images of 589×442 pixels, and divided into three categories according to the usages of machine learning, namely, training set (8×10^2 samples for each p_0), validation set (2×10^2 samples for each p_0), and test set (10^3 samples for each p_0). The input layer of the deep CNN employed has $3 \times 224 \times 224$ neurons (3 for RGB, and

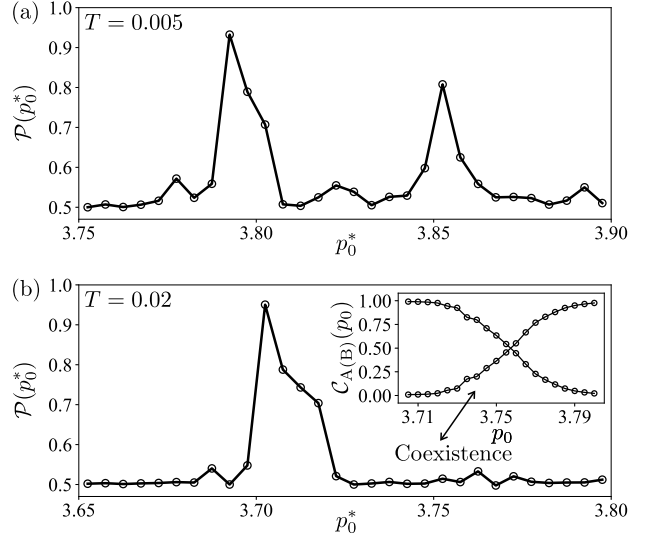


Figure S2. Analogous data to Figs. 1(b), (c), but employing another type of deep CNN called “GoogLeNet”. These results match very well with the ones obtained by the residual neural network. See text for more details.

224×224 is a standard input size), and the output layer has 2 neurons, i.e., y_A and y_B . The CNN is trained in both “scanning-probe” and “information-concealing” machine learning as a binary classifier that can extract the distinguishable features from the system’s spatial configurations and predict the class of the input samples. This prediction is compared to the given label of the sample and the error can be quantified by the cross-entropy cost function [1, 2]. The training of a CNN is realized by minimizing the cost function traversing the training set for several epochs. More specifically, the CNN is trained with the Adam optimization algorithm [3] starting from the pre-trained model using default settings in PyTorch. The auxiliary machine learning to resolve the hexatic-liquid phase coexistence is obtained by training and validating for 50 epoch traversing the samples and all the other results are obtained by training and validating for 5 epoch, repeating independently for 20 times to take the

* aibq@sncu.edu.cn

† liang.he@sncu.edu.cn

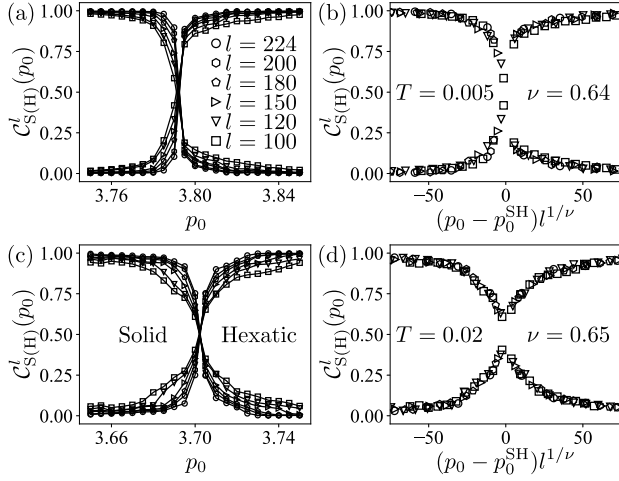


Figure S3. Analogous data to Figs. 2(b-e), but employing another type of deep CNN called “GoogLeNet”. These results also match very well with the ones obtained by the residual neural network. See text for more details.

average. For more thorough discussions on the machine learning techniques involved in the training process, we refer the reader to Refs. [1, 2].

BENCHMARK OF “INFORMATION-CONCEALING”

The “information-concealing” approach developed in this work is inspired by Refs. [4, 5], making use of the CNN to analyze the system’s spatial configurations from numerical simulations with particle number N fixed. Here, we present a benchmark of the “information-concealing” approach. We directly apply this approach to reveal the critical scaling of the correlation length in the vicinity of the ferromagnetic-paramagnetic transition of the 2D Ising model with the standard 18-layer residual neural network [6] employed to perform the classification tasks. The samples are generated from Monte Carlo simulations at different temperatures T in a square lattice of linear size $L = 224$ with periodic boundary condition imposed and without external field. Similar to what we have done in the main text, we first perform “concealing” with a choice of effective length scale l to generate the corresponding dataset. Then, this complete dataset is used to train the CNN to perform the classification between the ferromagnetic and the paramagnetic phases. After training, the CNN is able to output the classification confidence values (y_F, y_P) concerning the samples with corresponding temperature T , i.e., establish a map between the average confidence values ($\mathcal{C}_F, \mathcal{C}_P$), where $\mathcal{C}_{F(P)} \equiv \langle y_{F(P)} \rangle$, and the temperature T , from which the ferromagnetic-paramagnetic transition point, i.e., the so-called Curie temperature T_c , is identified by the T where $\mathcal{C}_F(T) = \mathcal{C}_P(T)$. We repeat this process with a series of different choices of the effective length scale

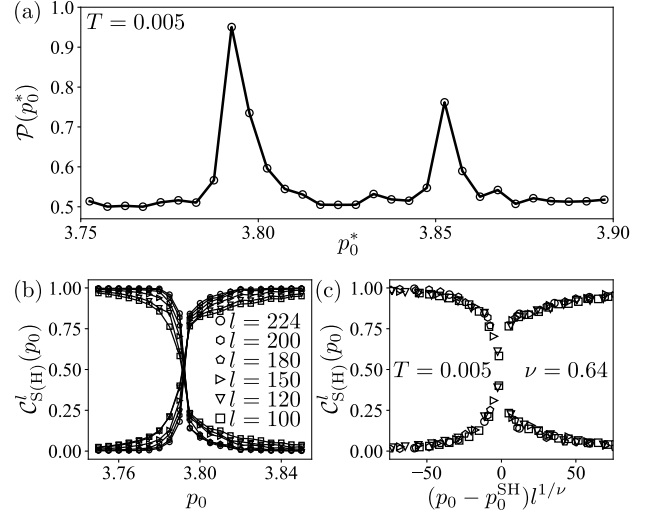


Figure S4. Analogous data to Figs. 1(b), 2(b), and 2(c), but using only half of the samples, i.e., only 10^3 for each p_0 at the low temperature $T = 0.005$. These results suggest that the number of samples used in the main text, i.e., 2×10^3 for each (T, p_0) , is large enough. See text for more details.

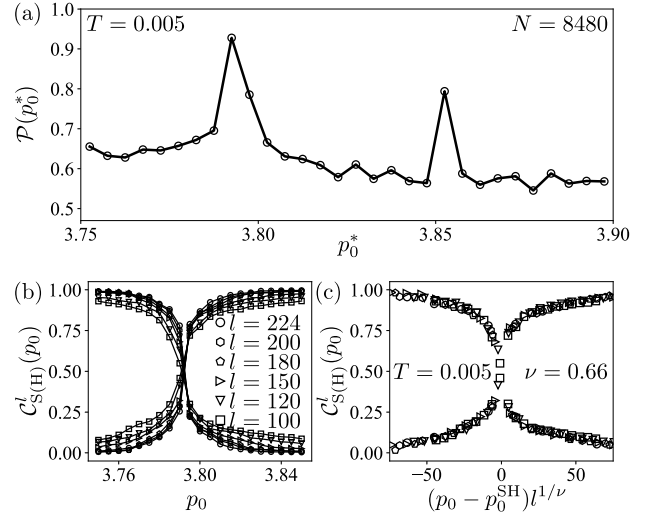


Figure S5. Analogous data to Figs. 1(b), 2(b), and 2(c), but considering a larger system size $N = 8480$. These results show that the finite size effect does not impose strong influences on the major results presented in the main text. See text for more details.

$l = 224, 200, 180, 150, 120, 100$, and get the corresponding $\mathcal{C}_F^l(T)$ and $\mathcal{C}_P^l(T)$. The average confidence values with different fixed l show the same dependence on its rescaled temperature $(T - T_c)l^{1/\nu_1}$ with $\nu_1 = 1.04$ in Fig. S1, indicating that the critical exponent ν_1 for the divergence of the correlation length of the ferromagnetic-paramagnetic transition assumes the value $\nu_1 = 1.04$, matching well with the exact value $\nu_1 = 1$ [7].

INDEPENDENCE ON THE CNN STRUCTURE

In the main text, we employ a standard 18-layer residual neural network [6] to perform the analysis as shown in Fig. 1 and Fig. 2. Here, we present the same analysis employing another type of deep CNN called “GoogLeNet” [8]. As we can see from Fig. S2, the “phase-transition-probe” realized by “GoogLeNet” detects the same phase transition points as the ones obtained by the residual neural network, and the upper bound for the hexatic phase region is estimated by the intersection point with $p_0^{\text{H,UB}} = 3.7573$ in the inset of Fig. S2(b). Fig. S3 shows the results of revealing the critical scaling of the solid-hexatic phase transition in deformable particles with “GoogLeNet” employed to perform the classification tasks, which also matches very well with “information-concealing” machine learning results obtained by the residual neural network in Fig. 2. We remark that these two deep CNNs have quite different structures, so the good consistency of the results clearly shows the CNN structure independence of both approaches developed in this work.

INFLUENCES OF THE FINITE SIZE EFFECT AND THE NUMBER OF SAMPLES IN THE DATASET

At a given temperature T , we have 6.2×10^4 samples in total. To investigate the influences of the num-

ber of samples in the dataset, here we use half of the samples, i.e., only 10^3 for each p_0 , to perform the same analysis at the low temperature $T = 0.005$. As we can see in Fig. S4(a), the “scanning-probe” machine learning identifies the solid-hexatic phase transition point $p_0^{\text{SH}} = 3.7925 \pm 0.0025$ and the hexatic-liquid phase transition point $p_0^{\text{HL}} = 3.8525 \pm 0.0025$, which are exactly the same as the ones obtained in Fig. 1(b) and Fig. S2(a). And the “information-concealing” machine learning extracts the critical exponent $\nu = 0.64$ in Fig. S4(c) for the divergence of the correlation length, which is also the same as the one obtained in Fig. 2(c) and Fig. S3(b). These results show that reducing the number of samples in the dataset by half from 6.2×10^4 to 3.1×10^4 does not impose noticeable influences on the major results, suggesting that the number of samples used in the main text, i.e., 2×10^3 for each (T, p_0) , is large enough.

Moreover, we also investigate the influences of the finite size effect, since it can be generally important in the melting transition of 2D systems [9]. Here, we consider a larger system size $N = 8480$, and find that the predicted phase transition points p_0^{SH} and p_0^{HL} are unchanged compared with the ones obtained in the main text [cf. Fig. S5(a) and Fig. 1(b)]. The critical exponent extracted via “information-concealing” machine learning is $\nu = 0.66$, which also agrees well with the results obtained in the main text [cf. Fig. S5(c) and Fig. 2(c)]. These results show that the finite size effect does not impose strong influences on the major results presented in the main text.

-
- [1] M. A. Nielsen, *Neural Networks and Deep Learning*, Determination Press (2015).
- [2] I. Goodfellow, Y. Bengio, and A. Courville, *Deep Learning*, MIT Press (2016).
- [3] D. P. Kingma and J. L. Ba, arXiv:1412.6980.
- [4] J. Carrasquilla and R. G. Melko, *Nat. Phys.* **13**, 431 (2017).
- [5] N. Maskara, M. Buchhold, M. Endres, and E. P. L. van Nieuwenburg, arXiv:2103.15855.
- [6] K. He, X. Zhang, S. Ren, and J. Sun, *Proc. of IEEE CVPR*, 770 (2016).
- [7] J. B. Kogut, *Rev. Mod. Phys.* **51**, 659 (1979).
- [8] C. Szegedy, W. Liu, Y. Jia, P. Sermanet, S. Reed, D. Anguelov, D. Erhan, V. Vanhoucke, and A. Rabinovich, *Proc. of IEEE CVPR*, 1 (2015).
- [9] P. S. Ruiz, Q.-L. Lei, and R. Ni, *Commun. Phys.* **2**, 70 (2019).